Co-option of Lysosomal Machinery for Biomineralization

Maitri Rangarajan-Paul,[1,*] Scott A. Nichols,[2] Martin Tresguerres[1,*]
[1] Scripps Institution of Oceanography, University of California San Diego, 9500 Gilman Drive, La Jolla, CA 92093, USA
[2] University of Denver, Department of Biological Sciences, 2101 E. Wesley Ave SGM 203, Denver, CO 80210-5210
[*]Correspondence: mapaul@ucsd.edu (M.R.P.), mtresguerres@ucsd.edu (M.T.)

Summary

Biomineralization first emerged ~600 million years ago, giving rise to novel strategies for buoyancy, locomotion, and defense.[1] Sponges are the only metazoans that build a silica-based skeleton,[2] and the cellular and molecular mechanisms underlying their silicification process are much less understood than in diatoms and land plants, the other two major biosilicifiers. Here, we show that the cells specialized for sponge biosilicification, termed sclerocytes, highly express lysosomal-associated genes, including the V-H^+-ATPase (VHA) proton pump, oculocutaneous albinism type 2 (OCA2) anion channels, cathepsin-L proteins, silicateins, TMEM55A, TMEM192, TMEM199, and multiple other proteins involved with lysosomal maintenance and degradation. Further, we demonstrate that VHA protein localizes to the sclerocyte silica deposition vesicle (SDV) and that VHA-dependent SDV acidification is essential for silica spicule formation. This function mirrors the localization and role of VHA in diatom biosilicification,[3] while in land plants, acidification occurs extracellularly in the xylem and is driven by a different proton pump, the plasma membrane P-type H^+-ATPase.[4,5] These results indicate that vesicle acidification is a shared mechanism for silica handling in sponges, diatoms, and plants. We also found that genes homologous to the plant silicon efflux transporter Lsi2,[6] which belong to the same gene family as OCA2,[7,8] are upregulated in sclerocytes. Using Hybridization Chain Reaction Fluorescence In Situ Hybridization (HCR-FISH), we found that sponge Lsi2 genes are expressed in sclerocytes, corroborating prior phylogenetic and transcriptomic evidence that Lsi2 homologs are involved in sponge and diatom silicic acid transport.[7–10] Taking into account previous work showing that VHA, cathepsins, and other lysosomal-associated genes have been associated with calcification across a remarkable range of eukaryotes including coccolitophores,[11] foraminifera,[12] sea urchins,[13] bryozoans,[14] crustaceans,[15] mollusks,[16] and mammals,[17] we posit that the various biomineralization mechanisms observed throughout the tree of life arose convergently through the co-option of an ancestral lysosomal gene toolkit.

Results and Discussion

Upregulation of lysosomal genes in sclerocytes

Analysis of single-cell RNA sequencing (RNASeq) data of demosponge *Spongilla lacustris*[18] revealed that mRNA transcripts of genes involved in lysosomal machinery were

upregulated (log2fold change > 1) in sclerocytes (Figure 1); including most subunits of VHA, an ATP-driven proton pump essential for lysosomal acidification,[19] OCA2, also known as the pink-eyed dilution protein or P protein,[20] which localizes to lysosome related organelles called melanosomes in vertebrate pigment-producing cells,[21,22] lysosomal cysteine protease cathepsin-L proteins, cathepsin L-like proteins called silicateins that have been found to involved in spiculogensis,[23] TMEM55A/B and TMEM192, proteins involved in lysosomal autophagy, phagocytosis, and lysosome repair,[24–26] TMEM199, a VHA assembly factor,[27] SNX8, a protein that enables lysosome reformation,[28]and CLIP4 and RNF11, proteins that mediate processes leading to lysosomal degradation.[29,30] VHA is highly conserved across all eukaryotes.[31] In addition to acidifying lysosomes, endosomes and phagosomes, VHA plays a critical role in diatoms silica cell wall formation by acidifying the silica deposition vesicle (SDV)[3]. Further, we found that two of the upregulated sponge genes annotated as OCA2 bore greater structural resemblance to plant silicon efflux transporter Lsi2 (Supplementary Figure 1A) and are thus referred to as sponge Lsi2 genes. Due to the links of VHA and Lsi2, to diatom and plant biosilicification, we specifically explored their roles in sponge biosilicification.

<u>VHA is abundant in sclerocytes and is essential for skeleton formation</u>

In recent decades, VHA has been shown to play a wide range of physiological roles in marine organsims.[3,32–39] Notably, VHA is essential for biosilicification in diatoms, allowing for silicic acid accumulation in the SDV.[3] The protein has been linked to biomineralization in calcifying organisms as well. In foraminifera, VHA maintains the proton flux responsible for calcification.[12] The gene has been shown to be upregulated in calcifying strains of coccolithophores.[11] A transcriptomic study on bryozoans identified VHA as a candidate biomineralization protein as it was upregulated in younger zooids, which are at the distal growth margin of the colony, compared to older zooids.[14] In sea urchins, VHA has been shown to play an essential role in skeleton re-calcification.[13] The protein also contributes to the mineralization-demineralization cycle of terrestrial isopods.[15]

Our analysis of published single-cell RNASeq data from *S. lacustris*[18] found that all subunits of VHA were upregulated in sclerocytes compared to other cell types, with the exception of integral domain V0 subunit e which was more highly expressed in myopeptidocytes (Supplementary Figure 2). However, this subunit does not seem to be essential for proton pump activity and may instead play a role in endomembrane specific VHA-assembly or targetting.[40] Some subunit isoforms such as V0 subunit a gene 3 and V0 subunit c gene 2 were specifically upregulated in sclerocytes compared to other cell types and compared to other isoforms suggesting that these isoforms may only localize to sclerocyte-specific organelles like the SDV. Immunostaining with specific antibodies against VHA subunit B (VHA_B) revealed a striking VHA localization within sclerocytes and around spicules in *S. lacustris* as well as in *Ephydatia muelleri* (Figure 2). In both cases, the VHA protein appeared to be surrounding

75 the SDV of sclerocytes, as well as within the cytoplasm, potentially on vesicles (Supplementary
76 Figure 3). Airyscan 'super-resolution' imaging showed VHA surrounding spicules fluorescently
77 labelled with PDMPO [2-(4-pyridyl)-5-((4-(2-dimethylaminoethylaminocarbamoyl)methoxy)-
78 phenyl)oxazole], an acidotropic dye that is selectively incorporated and co-deposited with Si
79 into the newly polymerized silica (Figure 3A).[41]
80 To test the functional role of VHA in spiculogenesis, sponges were incubated with the
81 specific pharmacological inhibitor of VHA, concanamycin (concA; 100 nM),[42,43] for 24 hours
82 along with PDMPO or with vehicle DMSO as a control (Figure 3B). VHA inhibition significantly
83 decreased the number of spicules per mm^2 of sponge tissue by 41.6% $\pm$ 10.6% in *E. muelleri* and
84 77.5% $\pm$ 7.1% in *S. lacustris*. The proportion of spicules labeled with PDMPO decreased by
85 85.8% $\pm$ 4.7% in *E. muelleri* and 98.3%$\pm$ 1.7% in *S. lacustris* indicating that spiculogenesis is
86 stunted by VHA inhibition (Figure 3C-D). Given that *S. lacustris* and *E. muelleri* are
87 phylogenetically distinct sponges with divergent life history, these observations suggest that
88 VHA-dependent silicification is a widespread, conserved mechanism in sponges (Figure 2, 3).
89 These results show that, as reported in diatoms[3], VHA-dependent SDV acidification is
90 critical for sponge biosilicification. By acidifying the SDV in both diatoms and sclerocytes, VHA
91 drives silicic acid accumulation and prevents its rapid polymerization into silica.[44,45] Given prior
92 evidence that VHA plays a role in calcification across a wide range of phyla, VHA appears to
93 have been co-opted independently by multiple lineages for biomineralization. Interestingly,
94 plants also use a proton pump to acidify the xylem sap where silicic acid is stored prior to
95 hardening. The xylem is acidified by the plant and fungi-specific[46] plasma membrane P-type H^+-
96 ATPase.[4,5] The co-option of proton pumps for maintenance of accumulated silicic acid appears
97 to be a shared feature for biosilicification over vastly diverged lineages.
98
99 <u>Lsi2 and OCA2 are highly expressed in sclerocytes</u>
100 Lsi2 and OCA2 belong to a family of transmembrane transporters with similarity to
101 SLC13. [7,8,47–49] Lsi2 is a silicic acid/H^+ antiporter that mediates silicic acid efflux into the plant
102 xylem.[6] OCA2 is a protein that localizes to melanosomes, lysosome related organelles, in
103 pigment-producing cells called melanocytes[21] which specifically occur in vertebrates.[22] These
104 proteins play a role in mediating chloride-selective anion conductance, providing charge
105 compensation and increasing proton-pumping efficiency of VHA.[50,51] A phylogenetic analysis of
106 the evolutionary history of Si transport reported that Lsi2 has homologs across a broad range of
107 eukaryotes which resolve into two main groups: one containing vertebrate OCA2-like
108 sequences, and the other containing the land plant Lsi2s together with Lsi2-like genes from
109 diverse prokaryotic and eukaryotic organisms.[7] This Lsi2-like clade was dominated by homologs
110 from silicifying organisms such as land plants, sponges, loricate choanoflagellates, haptophytes,
111 chrysophytes/synurophytes, radiolarians, and diatoms indicating that Lsi2-like genes play a role
112 in biosilicification. In alignment with this, Lsi2-like genes have been found to be upregulated in

113 marine hexactinellid sponge *Vazella pourtalesii* upon exposure to dissolved silicon.[8] In another
114 marine hexactinellid sponge *Aphrocallistes vastus*, an analysis of differentially expressed genes
115 between the osculum, the vertical growth zone where new skeletal growth is concentrated,[52]
116 and the main body, reported that Lsi2 was upregulated with other mineralization-related
117 genes.[9] There is also some transcriptomic evidence that an Lsi2-like gene may be involved in
118 silicic acid transport in diatoms.[10]
119 Our analysis of published single-cell RNASeq data from *S. lacustris*[18] showed that Lsi2
120 genes were upregulated in sclerocytes (Figure 4A). Alignment of the protein sequences of the
121 Lsi2 genes in *S. lacustris* and their equivalent homologs in *E. muelleri* against rice *Oryza sativa*
122 Lsi2 (*Os*Lsi2) showed that transmembrane regions are conserved (Supplementary Figure 1B).
123 OCA2 genes were also upregulated in sclerocytes but OCA2_1 was expressed in a smaller
124 percentage of sclerocyte cells than the Lsi2 genes and OCA2_2 was expressed in other cell types
125 as well indicating it may play a more generic housekeeping role in sponge lysosomes. Sponge
126 OCA2 genes may play a role similar to their function in vertebrate melanocytes of providing
127 counter-ion balance and improving efficiency of the VHA acidification mechanism. Notably, we
128 found that Lsi2 gene expression was much higher in sclerocytes than the previously described
129 sponge silicic acid uptake protein the $\{Na^+/HCO_3^-[Si(OH)_4]\}$ co-transporter or NBCSA,[53] (Figure
130 4A) which matches recent claims that NBCSA is not critical for silicic acid transport in all
131 sponges.[8] Confirming the single-cell RNASeq data, HCR-FISH probes designed against the Lsi2
132 genes in *S. lacustris* and *E. muelleri* distinctly labeled sclerocytes (Figure 4B). Interestingly, the
133 two Lsi2 homologs showed heterogeneous expression in sclerocytes: i.e. Lsi2_1 signal was
134 stronger in some sclerocytes, while Lsi2_2 signal was stronger in others; overall, Lsi2_2 was
135 more ubiquitously expressed around spicules than Lsi2_1 (Supplementary Figure 4). As we only
136 visualized mRNA, we could not definitively conclude whether the Lsi2 proteins localize to the
137 SDV membrane or the plasma membrane. We attempted to design antibodies against these
138 proteins but were unsuccessful. However, we speculate that they would localize to the SDV
139 membrane as the Lsi2 silicic acid/H^+ antiporter activity relies on a proton gradient and VHA
140 would only be able to pump H^+ ions from the cytosol to an intracellular compartment.[54]
141 These findings strongly suggest that the Lsi2 genes are involved in sponge silicic acid
142 uptake. The dependance of Lsi2 on an acidification mechanism and the critical role of OCA2 in a
143 lysosome-related organelle, point to lysosomal origins of a gene family with clear association to
144 sponge spiculogenesis.
145
146 <u>Links between lysosomal detoxification and biomineralization</u>
147 In their phylogenetic analysis of silicon transport genes, Marron *et al*. propose that the Lsi2
148 protein evolved in the original eukaryote as a detoxification mechanism to export silicic acid out
149 of cells in the high Si oceans of the Precambrian to prevent uncontrolled silica deposition and
150 were later co-opted for biosilicification by a specific set of lineages at the

151 Precambrian/Cambrian boundary.[7] This hypothesis implies a switch of Lsi2 orientation within
152 the membrane from exporting silicic acid out of cells to transporting it in. However, it is
153 possible that Lsi2 detoxified silicic acid by sequestering it within lysosomes rather than by
154 pumping it out of cells. Such a mechanism would seamlessly lend itself to the accumulation of
155 silicic acid into the SDV of diatoms and sponges, while also inserting at the plasma membrane
156 of plant cells in an orientation that mediates silicic acid extrusion into the xylem.
157 Lysosomes and detoxification are intrinsically linked. For example, calcium and heavy metal
158 ions including zinc, copper, and iron are sequestered in lysosomes and vacuoles in many
159 invertebrate phyla into structures termed concretions or granules, rendering them insoluble
160 and detoxified.[55–62] These organelles are often acidified by VHA.[63,64] The sequestered
161 concretions found in oysters,[56] bivalves,[58] snails,[59,60] insects,[61] and crustaceans[55,64] could be
162 considered precursors to skeletons. In fact, it has been proposed that metal detoxification was
163 a selective pressure that shaped the evolution of biomineralization.[65–67] Calcium ions are
164 disruptive to cellular functioning as their precipitation intracellularly would be deleterious;
165 therefore, sequestration within a pre-existing acidified organelle may have provided an
166 energetically effective solution,[65] while also offering a parsimonious mechanistic explanation at
167 the evolutionary level. Recently, it was shown that osteoblasts, cells responsible for secreting
168 calcium phosphate mineral precursors for bone formation, transport amorphous calcium
169 phosphate via lysosomes.[17] Additionally, pharmacological inhibition of VHA prevented the
170 formation of electron-dense granules and extracellular calcified nodules,[17] matching the
171 importance of VHA for silicification in sponges (current study) and in diatoms. [3] Furthermore,
172 other studies have shown that increased expression of the master regulator of lysosomal
173 biogenesis, *Tfeb*, enhances osteoblastic differentiation[68] and increases bone mass and
174 strength.[69] Altogether, the evidence suggests that ancient links between detoxification and
175 lysosomal machinery set the stage for the repeated evolution of biomineralization.
176
177 <u>Lysosomal machinery as part of ancestral genetic toolkit for biomineralization</u>
178 It has been proposed that genes involved in biomineralization were independently co-
179 opted from an ancestral genetic toolkit,[70] however, the specific genes within this toolkit have
180 not been clearly identified. Here, we found high expression of lysosomal genes in sclerocytes
181 including cathepsins, silicateins, TMEM55A/B, TMEM192, and TMEM199. Cathepsins are
182 lysosomal proteases speculated to play a role in making precise cuts in matrix and
183 mineralization proteins for the process of biosilicification.[9] They are upregulated during shell
184 repair in mussels,[16] cathepsin B/X has been identified in sea urchin spine extracts,[71] and our
185 analysis of single-cell RNASeq dataset of a stony coral revealed that cathepsin L and cathepsin V
186 are upregulated in skeleton-forming cells, calicoblasts.[72] Silicatein was discovered in the protein
187 filaments of spicules from demosponge *Tethya aurantia.*[23] Silicateins are highly similar to
188 members of the cathepsin L and papain family of proteases, but the cysteine at the active site in

189 the proteases is replaced by serine.[23] They have been proposed to retain protease activity
190 similar to other cathepsins,[73] catalyze the polymerization of silicic acid, [74] or serve as scaffolding
191 for spicule formation.[75] TMEM55A/B and TMEM192, involved in lysosomal autophagy,
192 phagocytosis, and lysosome repair,[24–26] and TMEM199,[27] a VHA assembly factor, have not been
193 previously described within the context of biosilicification to our knowledge. We found
194 upregulation of VHA mRNA in sclerocytes, VHA protein localization around spicules, and
195 showed that inhibition of VHA disrupts skeleton formation. This aligns with similar findings on
196 biosilicification in diatoms,[3] and calcification in bryozoans,[14] sea urchins,[13] foraminifera,[12]
197 coccolitophores,[11] and crustaceans.[15] We report that Lsi2 genes were upregulated in sponge
198 sclerocytes, likely playing a role in silicic acid uptake similar to plants.[6] In the marine
199 hexactinellid sponge *Aphrocallistes vastus*, VHA, Lsi2, and various cathepsins were upregulated
200 in the osculum region of indicating a potential link to sponge skeleton formation.[9] Exposure of
201 hexactinellid sponge *Vazella pourtalesii* to dissolved silicon (DSi), led to the upregulation of
202 cathepsins and Lsi2.[8] Further, a proteomic analysis found that spicule contents of marine
203 demosponge *Petrosia ficiformis* were dominated by proteins involved in lysosomal function
204 including cathepsins and silicatein.[76] While these studies used methods of bulk RNASeq and
205 proteomics of isolated spicules, a major advance of our study is the usage of single-cell RNASeq
206 data, *in situ* protein and mRNA localization, and functional assays to conclusively show the
207 importance of lysosomal genes in sponge skeleton formation. The machinery responsible for
208 the biogenesis of lysosome-related organelles is present across the eukaryotic tree of life and is
209 likely to have been in place prior to the last eukaryotic common ancestor.[77] Given that
210 lysosomal genes have been shown to be involved in biomineralization across a broad sweep of
211 taxa, the combined evidence suggest that lysosomal machinery was co-opted independently
212 multiple times for skeleton formation, forming a key set of genes within the ancestral toolkit for
213 biomineralization.
214
215 **Conclusion**
216 Skeleton formation was a key innovation that catapulted the trajectory of body plan
217 evolution during the Cambrian. It provided organisms with new possibilities for protection,
218 support, locomotion, and defense.[1] Biomineralization is intrinsically linked with global calcium
219 and silica cycling. Importantly, many marine organisms are ballasted by their silica and calcium
220 skeletons for burial in the seafloor, allowing for carbon sequestration.[78,79] Here, we describe the
221 co-option of lysosomal genes for biosilicification in sponges, the earliest diverged branch of
222 metazoans.[80] We discuss parallels to biomineralization pathways across the tree of life, from
223 protists to mammals. Although biomineralization evolved independently multiple times, the co-
224 option of genes from a conserved toolkit is remarkable.[70] Our findings provide novel evidence
225 for the co-option of ancestral lysosomal machinery for biomineralization.
226

227 **Methods**

228 *Organisms*

229 *Ephydatia muelleri* and *Spongilla lacustris* gemmules were obtained from the Nichols
230 lab. They were collected from the upper peninsula of Michigan in 2023. Gemmules were stored
231 at 4°C and hatched in spring water (Crystal Geyser) at room temperature in cover-slip bottom
232 dishes as previously described[81].
233

234 *RNASeq analysis*

235 Datasets acquired from Musser et al[18] and used Seurat in R to plot the expression of
236 sclerocytes markers. We referenced the *S. lacustris* transcriptome and proteome provided in
237 Musser et al[18] to identify homologs and design HCR-FISH probes. R code and lists of *S. lacustris*
238 genes analyzed can be found in our github repository.
239

240 *Antibodies*

241 Sponges were probed for VHA using a custom rabbit polyclonal antibody developed
242 using a peptide antigen matching a conserved region of VHA's B subunit (VHA_B;
243 AREEVPGRRGFPGY; GenScript Biotech Corporation, Piscataway, NJ, USA) which is conserved in
244 species ranging from sponges to humans.[34,35,82–84] We confirmed the epitope is 100% conserved
245 in *E. muelleri* and *S. lacustris* (Supplementary Figure 5A).
246

247 *Immunohistochemistry*

248 Immunohistochemical localization of anti-VHA_B antibody in sponges was done following
249 previously described protocol.[85] Briefly, 4-7 day old gemmule-hatched *E. muelleri* and *S.*
250 *Lacustris* sponges were fixed with 4% paraformaldehyde in 95% EtOH for 45 minutes at room
251 temperature. Sponges were rinsed with 0.1% Tween 20 (v/v) in phosphate buffered saline
252 (PTw) three times before incubation with blocking buffer (3% Bovine Albumin Serum in PTw) for
253 45 minutes at room temperature. Samples were incubated overnight (4°C) with either 0.962 µg
254 ml^{-1} polyclonal anti-VHA_B primary antibody in blocking buffer or 0.962 µg ml^{-1} polyclonal anti-
255 VHA_B primary antibody with 60x peptide as a "peptide preabsorption control". Sponges were
256 rinsed with PTw three times and subsequently incubated with 4 µg ml^{-1} secondary antibody
257 (goat anti–rabbit–Alexa Fluor 488; A-11008; Invitrogen, Carlsbad, CA, USA) and 4 µg ml^{-1} 4',6-
258 diamidino-2-phenylindole (DAPI) DNA stain (Invitrogen) in blocking buffer for 45 minutes in the
259 dark at room temperature. Excess secondary antibody and DAPI were washed from samples by
260 rinsing three times with PTw and they were mounted for imaging using ProLong Glass Antifade
261 Mountant (P36982; Invitrogen). Confocal microscopy was performed on a Zeiss AxioObserver
262 Z1 connected to a laser scanner equipped with 405, 488, 561, and 640 nm laser lines (Zeiss LSM
263 800 with Airyscan, Carl Zeiss AG, Oberkochen, Baden-Württemberg, Germany). Samples were
264 imaged with the following excitation and emission wavelengths: Alexa Fluor 488 — ex: 488 nm,
265 em: 488-561 nm; DAPI—ex: 405 nm, em: 400-488 nm.
266

267 *Western blots*

268 Custom polyclonal antibodies against VHA subunit B (VHA_B) were used to investigate
269 VHA localization in sponge tissues of demosponges *Ephydatia muelleri* and *Spongilla lacustris*.

270 Approximately 50-80 *E. muelleri* and *S. lacustris* gemmules were hatched in separate
271 petri dishes. At 9-11 days old, sponges were scraped off the dishes with a razor blade and
272 dounce homogenized in 100 µL of 1x protease inhibitor cocktail (P2714; Sigma-Aldrich) in spring
273 water. Samples were sonicated for 3x10 second bursts with 1-minute rests on ice.
274 Homogenates were spun down for two minutes and the supernatant was retained. The protein
275 concentrations of samples were obtained using Bradford assay performed with a bovine serum
276 albumin standard curve (BioRad, Hercules, CA, USA). Samples were incubated in Laemmli
277 Sample buffer with 5% (v/v) β-mercaptoethanol for 5 min at 100 °C and increasing amounts of
278 protein were loaded into a sodium dodecyl sulphate–polyacrylamide gel electrophoresis gel in
279 duplicate (*E. muelleri*: 0.7 µg, 3.5 µg, 7 µg, 13.9 µg; *S. lacustris*: 0.7 µg, 3.5 µg, 7 µg, 13.9 µg).
280 The gel was run in in Tris-glycine running buffer (25 mM Tris-base, 192 mM glycine, 0.1% (w/v)
281 sodium dodecyl sulphate, pH 8.3; Sigma-Aldrich) at 47V for 35 minutes followed by 150V for 35-
282 40 minutes until the proteins had reached the bottom of the gel. Proteins were transferred
283 from the gel onto a polyvinylidene difluoride (PVDF) membrane using a Mini Tans-Blot Cell (Bio-
284 Rad) filled with Towbin transfer buffer (25 mM Tris, 192 mM glycine, 20% (v/v) methanol, pH
285 8.3; Sigma-Aldrich) at 90 mAmps overnight. PVDF membranes were incubated with blocking
286 buffer (1g non-fat dry milk powder in 10 mls Tris-buffered saline with 0.1% Tween (TBS-T)) for 1
287 hour at room temperature on an orbital shaker and subsequently incubated overnight at 4 °C
288 with either 0.2405 µg/mL anti-VHA_B primary antibody or anti-VHA_B primary antibody with 60x
289 excess peptide ("peptide preabsorption control") in blocking buffer. Membranes were washed
290 with 3 x 10 min TBS-T and then incubated with secondary antibody (goat anti–rabbit–
291 horseradish peroxidase diluted 1:5000; Bio-Rad) for 1 hour on an orbital shaker at room
292 temperature. Membranes were washed again with 3 x 10 min TBS-T and imaged with Clarity
293 Max Western ECL Substrate (Bio-Rad) using a Chemidoc Imaging system (Bio-Rad). Western
294 blotting specifically detected the expected ~55 kDa band (Supplementary Figure 5B).
295
296 *HCR-FISH protocol*
297 Probes were designed using publicly available HCR-FISH probe generator.[86–89] Sequences
298 against which probes were designed are provided in supplementary table 2. *E. muelleri* Lsi2
299 homologs were identified by blasting Lsi2 sequences against an unpublished transcriptome. 6-
300 10 day old gemmule-hatched *E. muelleri* and *S. Lacustris* sponges were stained using HCR FISH
301 probes following an adapted previously described protocol.[90] Briefly, sponges were fixed in cold
302 4% PFA in 1/4x HF buffer (147.5mM NaCl, 0.1675 mM KCl, 0.19 mM $CaCl_2$, 0.06mM NaHCO in
303 RNAse-free water) on a gently rocking platform at 4C overnight. Samples were rinsed with ¼ x
304 HF buffer and then incubated with ¼ x HF buffer containing an RNAse inhibitor (1 U/µl final
305 concentration) at room temperature for 10 minutes. Sponges were rinsed again with ¼ x HF
306 buffer and progressively dehydrated into 100% methanol. Subsequently, 100% methanol was
307 replaced with 100% ethanol, sponges were progressively rehydrated into 0.1% Tween 20 (v/v)
308 in phosphate buffered saline (PTw) and incubated with of 5 µg/mL Proteinase K in PTw for 90
309 seconds at room temperature. The proteinase K solution was removed and sponges were
310 incubated with 2mg/ml glycine in PTw for 5 minutes at room temperature twice. Samples were
311 rinsed with PTw and re-fixed with 4% PFA in PTw for one hour at room temperature. Following
312 two rinses with PTw, samples were incubated with 2x Saline Sodium Citrate (SSC) for 10
313 minutes at room temperature twice. Sponges were then pre-hybridized by incubation with

314 Hybridization buffer (Molecular Instruments), first at room temperature for 10 minutes and
315 then at 37°C for 30 minutes. Subsequently, samples were incubated with 0.04 µM probe in
316 hybridization buffer or just hybridization buffer for the "no probe, hairpin only control"
317 (Supplemnetary figure 6) at 37°C overnight. Sponges were rinsed with probe wash buffer
318 (Molecular Instruments) for 5 mins at 37°C three times, then incubated with 2x SSC for 5
319 minutes at room temperature twice. Samples were pre-amplified with amplification buffer
320 (Molecular Instruments) for 5 minutes at room temperature twice, then incubated with 60 nM
321 of snapcooled (incubated at 95°C for 90 seconds, then cooled in the dark for at least 30
322 minutes) hairpins (Molecular Instruments) in amplification buffer at room temperature in the
323 dark overnight. Specimens were rinsed with 2x SSC for 5 minutes at room temperature twice.
324 2x SSC was replaced with 10 µg ml^{-1} 4',6-diamidino-2-phenylindole (DAPI) in PBS for 20 minutes
325 at room temperature. Sponges were rinsed with PBS and then mounted using ProLong Glass
326 Antifade Mountant (P36982; Invitrogen). Confocal microscopy was performed on a Zeiss
327 AxioObserver Z1 connected to a laser scanner equipped with 405, 488, 561, and 640 nm laser
328 lines (Zeiss LSM 800 with Airyscan, Carl Zeiss AG, Oberkochen, Baden-Württemberg, Germany).
329 Samples were imaged with the following excitation and emission wavelengths: Alexa Fluor 555
330 — ex: 561 nm, em: 561- 585 nm; Alexa Fluor 488 — ex: 488 nm, em: 488-561 nm; DAPI—ex:
331 405 nm, em: 400-488 nm.
332
333 *PDMPO experiments*
334 4-11 day old gemmule-hatched *E. muelleri* and *S. Lacustris* sponges were incubated with
335 1 uM PDMPO [2-(4-pyridyl)-5-((4-(2-
336 dimethylaminoethylaminocarbamoyl)methoxy)phenyl)oxazole] or LysoSensor Yellow/Blue
337 DND-160 (Invitrogen L7545) and either 100nM concanamycinA (concA) or an equivalent volume
338 of DMSO for 24 hours (*E. muelleri* n=4 and *S. lacustris* n=3 for each condition). PDMPO
339 fluorescence (ex: 405 nm, em: 490-515 nm) and brightfield images were taken in five 0.408
340 mm^2 regions around the periphery of each sponge. The number of spicules per region and the
341 number of spicules per region exhibiting PMDPO fluorescence were counted in ImageJ. The
342 proportion of spicules with PDMPO fluorescence was calculated by dividing number of spicules
343 exhibiting PDMPO fluorescence by the total number of spicules per region. The number of
344 spicules per mm^2 and the proportion of spicules with PDMPO were averaged across regions to
345 get the final mean values per sponge. The statistical differences for both aforementioned
346 parameters between sponges treated with concA versus DMSO were calculated using a student
347 t-test. Stereoscope images of all sponges in the experiment were taken before and after
348 treatment to confirm viability of the sponges (Supplementary Figure 6).
349
350 Resource Availability
351 Lead Contact
352 Requests for further information and resources should be directed to and will be fulfilled by the
353 lead contact, Maitri Rangarajan-Paul (mapaul@ucsd.edu).
354
355 Materials availability
356 Antibodies used for immunostaining of sponges will be shared by the lead contact upon
357 request.

Data and Code availability

Data and code used in this study are available at https://github.com/maitripaul/Co-option-of-Lysosomal-Machinery-for-Biomineralization

Acknowledgments

We thank Jake Pawley and Haley Womack for their assistance in providing us with sponge gemmules and advice on sponge-rearing. M.R.P. was funded by NSF-GRFP 2023360321.

Author contributions

Conceptualization: M.R.P., M.T.; Data curation: M.R.P., S.N.; Formal analysis: M.R.P., S.N., M.T.; Funding acquisition: M.R.P., M.T.; Investigation: M.R.P.; Methodology: M.R.P., S.N., M.T.; Project administration: M.R.P., M.T.; Resources: S.N., M.T.; Software: M.R.P.; Supervision: M.T.; Validation: M.R.P.; Visualization: M.R.P., S.N., M.T.; Writing – original draft: M.R.P., M.T.; Writing – editing: M.R.P., S.N., M.T.

Declaration of interests

The authors declare no competing interests.

References

1. Gilbert, P.U.P.A., Bergmann, K.D., Boekelheide, N., Tambutté, S., Mass, T., Marin, F., Adkins, J.F., Erez, J., Gilbert, B., Knutson, V., et al. (2022). Biomineralization: Integrating mechanism and evolutionary history. Science Advances *8*, eabl9653. https://doi.org/10.1126/sciadv.abl9653.

2. Müller, W.E.G., Wang, X., Cui, F.-Z., Jochum, K.P., Tremel, W., Bill, J., Schröder, H.C., Natalio, F., Schloßmacher, U., and Wiens, M. (2009). Sponge spicules as blueprints for the biofabrication of inorganic–organic composites and biomaterials. Appl Microbiol Biotechnol *83*, 397–413. https://doi.org/10.1007/s00253-009-2014-8.

3. Yee, D.P., Hildebrand, M., and Tresguerres, M. (2020). Dynamic subcellular translocation of V-type H+-ATPase is essential for biomineralization of the diatom silica cell wall. New Phytologist *225*, 2411–2422. https://doi.org/10.1111/nph.16329.

4. Jahn, T., Baluska, F., Michalke, W., Harper, J.F., and Volkmann, D. (1998). Plasma membrane H+-ATPase in the root apex: Evidence for strong expression in xylem parenchyma and asymmetric localization within cortical and epidermal cells. Physiologia Plantarum *104*, 311–316. https://doi.org/10.1034/j.1399-3054.1998.1040304.x.

5. Sattelmacher, B. (2001). The apoplast and its significance for plant mineral nutrition. New Phytologist *149*, 167–192. https://doi.org/10.1046/j.1469-8137.2001.00034.x.

6. Ma, J.F., Yamaji, N., Mitani, N., Tamai, K., Konishi, S., Fujiwara, T., Katsuhara, M., and Yano, M. (2007). An efflux transporter of silicon in rice. Nature *448*, 209–212. https://doi.org/10.1038/nature05964.

397 7. Marron, A.O., Ratcliffe, S., Wheeler, G.L., Goldstein, R.E., King, N., Not, F., de Vargas, C., and
398 Richter, D.J. (2016). The Evolution of Silicon Transport in Eukaryotes. Mol Biol Evol *33*, 3226–
399 3248. https://doi.org/10.1093/molbev/msw209.

400 8. Maldonado, M., López-Acosta, M., Beazley, L., Kenchington, E., Koutsouveli, V., and Riesgo,
401 A. (2020). Cooperation between passive and active silicon transporters clarifies the
402 ecophysiology and evolution of biosilicification in sponges. Science Advances *6*, eaba9322.
403 https://doi.org/10.1126/sciadv.aba9322.

404 9. Francis, W.R., Eitel, M., Vargas, S., Garcia-Escudero, C.A., Conci, N., Deister, F., Mah, J.L.,
405 Guiglielmoni, N., Krebs, S., Blum, H., et al. (2023). The genome of the reef-building glass
406 sponge Aphrocallistes vastus provides insights into silica biomineralization. Royal Society
407 Open Science *10*, 230423. https://doi.org/10.1098/rsos.230423.

408 10. Shrestha, R.P., Tesson, B., Norden-Krichmar, T., Federowicz, S., Hildebrand, M., and Allen,
409 A.E. (2012). Whole transcriptome analysis of the silicon response of the diatom Thalassiosira
410 pseudonana. BMC Genomics *13*, 499. https://doi.org/10.1186/1471-2164-13-499.

411 11. Mackinder, L., Wheeler, G., Schroeder, D., von Dassow, P., Riebesell, U., and Brownlee, C.
412 (2011). Expression of biomineralization-related ion transport genes in Emiliania huxleyi.
413 Environmental Microbiology *13*, 3250–3265. https://doi.org/10.1111/j.1462-
414 2920.2011.02561.x.

415 12. Toyofuku, T., Matsuo, M.Y., de Nooijer, L.J., Nagai, Y., Kawada, S., Fujita, K., Reichart, G.-J.,
416 Nomaki, H., Tsuchiya, M., Sakaguchi, H., et al. (2017). Proton pumping accompanies
417 calcification in foraminifera. Nat Commun *8*, 14145. https://doi.org/10.1038/ncomms14145.

418 13. Hu, M.Y., Petersen, I., Chang, W.W., Blurton, C., and Stumpp, M. (2020). Cellular
419 bicarbonate accumulation and vesicular proton transport promote calcification in the sea
420 urchin larva. Proceedings of the Royal Society B: Biological Sciences *287*, 20201506.
421 https://doi.org/10.1098/rspb.2020.1506.

422 14. Achilleos, K., Smith, A.M., Kenny, N.J., and Brown, C.M. (2024). A new transcriptome
423 resource for Cellaria immersa (Phylum: Bryozoa) reveals candidate genes and proteins
424 related to biomineralization. Front. Mar. Sci. *11*.
425 https://doi.org/10.3389/fmars.2024.1389708.

426 15. Ziegler, A., Weihrauch, D., Hagedorn, M., Towle, D.W., and Bleher, R. (2004). Expression and
427 polarity reversal of V-type H+-ATPase during the mineralization–demineralization cycle in
428 Porcellio scabersternal epithelial cells. J Exp Biol *207*, 1749–1756.
429 https://doi.org/10.1242/jeb.00953.

430 16. Yarra, T., Ramesh, K., Blaxter, M., Hüning, A., Melzner, F., and Clark, M.S. (2021).
431 Transcriptomic analysis of shell repair and biomineralization in the blue mussel, Mytilus
432 edulis. BMC Genomics *22*, 437. https://doi.org/10.1186/s12864-021-07751-7.

433 17. Iwayama, T., Okada, T., Ueda, T., Tomita, K., Matsumoto, S., Takedachi, M., Wakisaka, S.,
434 Noda, T., Ogura, T., Okano, T., et al. (2019). Osteoblastic lysosome plays a central role in
435 mineralization. Sci Adv *5*, eaax0672. https://doi.org/10.1126/sciadv.aax0672.

436 18. Musser, J.M., Schippers, K.J., Nickel, M., Mizzon, G., Kohn, A.B., Pape, C., Ronchi, P.,
437 Papadopoulos, N., Tarashansky, A.J., Hammel, J.U., et al. (2021). Profiling cellular diversity in
438 sponges informs animal cell type and nervous system evolution. Science *374*, 717–723.
439 https://doi.org/10.1126/science.abj2949.

440 19. Mindell, J.A. (2012). Lysosomal Acidification Mechanisms*. Annual Review of Physiology *74*,
441 69–86. https://doi.org/10.1146/annurev-physiol-012110-142317.

442 20. H. Brilliant, M. (2001). The Mouse p (pink-eyed dilution) and Human P Genes,
443 Oculocutaneous Albinism Type 2 (OCA2), and Melanosomal pH. Pigment Cell Research *14*,
444 86–93. https://doi.org/10.1034/j.1600-0749.2001.140203.x.

445 21. Sitaram, A., Piccirillo, R., Palmisano, I., Harper, D.C., Dell'Angelica, E.C., Schiaffino, M.V., and
446 Marks, M.S. (2009). Localization to Mature Melanosomes by Virtue of Cytoplasmic Dileucine
447 Motifs Is Required for Human OCA2 Function. MBoC *20*, 1464–1477.
448 https://doi.org/10.1091/mbc.e08-07-0710.

449 22. Sauka-Spengler, T., and Bronner-Fraser, M. (2008). A gene regulatory network orchestrates
450 neural crest formation. Nat Rev Mol Cell Biol *9*, 557–568. https://doi.org/10.1038/nrm2428.

451 23. Shimizu, K., Cha, J., Stucky, G.D., and Morse, D.E. (1998). Silicatein α: Cathepsin L-like
452 protein in sponge biosilica. Proceedings of the National Academy of Sciences *95*, 6234–6238.
453 https://doi.org/10.1073/pnas.95.11.6234.

454 24. Morioka, S., Nigorikawa, K., Okada, E., Tanaka, Y., Kasuu, Y., Yamada, M., Kofuji, S.,
455 Takasuga, S., Nakanishi, H., Sasaki, T., et al. (2018). TMEM55a localizes to macrophage
456 phagosomes to downregulate phagocytosis. J Cell Sci *131*, jcs213272.
457 https://doi.org/10.1242/jcs.213272.

458 25. Jeong, E., Willett, R., Rissone, A., La Spina, M., and Puertollano, R. (2024). TMEM55B links
459 autophagy flux, lysosomal repair, and TFE3 activation in response to oxidative stress. Nat
460 Commun *15*, 93. https://doi.org/10.1038/s41467-023-44316-6.

461 26. Nguyen, T.L., Schneppenheim, J., Rudnik, S., Lüllmann-Rauch, R., Bernreuther, C., Hermans-
462 Borgmeyer, I., Glatzel, M., Saftig, P., and Schröder, B. (2017). Functional characterization of
463 the lysosomal membrane protein TMEM192 in mice. Oncotarget *8*, 43635–43652.
464 https://doi.org/10.18632/oncotarget.17514.

465 27. Miles, A.L., Burr, S.P., Grice, G.L., and Nathan, J.A. (2017). The vacuolar-ATPase complex and
466 assembly factors, TMEM199 and CCDC115, control HIF1α prolyl hydroxylation by regulating
467 cellular iron levels. eLife *6*, e22693. https://doi.org/10.7554/eLife.22693.

468 28. Li, X., Xiang, C., Zhu, S., Guo, J., Liu, C., Wang, A., Cao, J., Lu, Y., Neculai, D., Xu, P., et al.
469 (2024). SNX8 enables lysosome reformation and reverses lysosomal storage disorder. Nat
470 Commun *15*, 2553. https://doi.org/10.1038/s41467-024-46705-x.

471 29. Tang, T., Yang, Z., Wang, D., Yang, X., Wang, J., Li, L., Wen, Q., Gao, L., Bian, X., and Yu, S.
472 (2020). The role of lysosomes in cancer development and progression. Cell Biosci *10*, 131.
473 https://doi.org/10.1186/s13578-020-00489-x.

474 30. Mattioni, A., Boldt, K., Auciello, G., Komada, M., Rappoport, J.Z., Ueffing, M., Castagnoli, L.,
475 Cesareni, G., and Santonico, E. (2020). Ring Finger Protein 11 acts on ligand-activated EGFR
476 via the direct interaction with the UIM region of ANKRD13 protein family. The FEBS Journal
477 *287*, 3526–3550. https://doi.org/10.1111/febs.15226.

478 31. Kibak, H., Taiz, L., Starke, T., Bernasconi, P., and Gogarten, J.P. (1992). Evolution of structure
479 and function of V-ATPases. J Bioenerg Biomembr *24*, 415–424.
480 https://doi.org/10.1007/BF00762534.

481 32. Tresguerres, M. (2016). Novel and potential physiological roles of vacuolar-type H+-ATPase
482 in marine organisms. J Exp Biol *219*, 2088–2097. https://doi.org/10.1242/jeb.128389.

483 33. Tresguerres, M., Parks, S.K., Wood, C.M., and Goss, G.G. (2007). V-H+-ATPase translocation
484 during blood alkalosis in dogfish gills: interaction with carbonic anhydrase and involvement
485 in the postfeeding alkaline tide. American Journal of Physiology-Regulatory, Integrative and
486 Comparative Physiology *292*, R2012–R2019. https://doi.org/10.1152/ajpregu.00814.2006.

487 34. Tresguerres, M., Katz, S., and Rouse, G.W. (2013). How to get into bones: proton pump and
488 carbonic anhydrase in Osedax boneworms. Proceedings of the Royal Society B: Biological
489 Sciences *280*, 20130625. https://doi.org/10.1098/rspb.2013.0625.

490 35. Barott, K.L., Venn, A.A., Perez, S.O., Tambutté, S., and Tresguerres, M. (2015). Coral host
491 cells acidify symbiotic algal microenvironment to promote photosynthesis. Proceedings of
492 the National Academy of Sciences *112*, 607–612. https://doi.org/10.1073/pnas.1413483112.

493 36. Barott, K.L., Thies, A.B., and Tresguerres, M. (2022). V-type H+-ATPase in the symbiosome
494 membrane is a conserved mechanism for host control of photosynthesis in anthozoan
495 photosymbioses. Royal Society Open Science *9*, 211449.
496 https://doi.org/10.1098/rsos.211449.

497 37. Thies, A.B., Rangarajan-Paul, M., Wangpraseurt, D., and Tresguerres, M. (2025). Co-option
498 of immune and digestive cellular machinery to support photosymbiosis in amoebocytes of
499 the upside-down jellyfish Cassiopea xamachana. Journal of Experimental Biology *228*,
500 jeb249849. https://doi.org/10.1242/jeb.249849.

501 38. Hargadon, A.C., Viliunas, J.W., Koehler, S., Thies, A.B., Chen, G.Y., Ladinsky, M.S., Kuwabara,
502 J., Avila-Magana, V., Ruby, E.G., Tresguerres, M., et al. (2024). An acidic microenvironment

503 produced by the V-type ATPase of Euprymna scolopes promotes specificity during Vibrio
504 fischeri recruitment. Commun Biol *7*, 1642. https://doi.org/10.1038/s42003-024-07348-2.

505 39. Allard, C.A.H., Thies, A.B., Mitra, R., Vaelli, P.M., Leto, O.D., Walsh, B.L., Laetz, E.M.J.,
506 Tresguerres, M., Lee, A.S.Y., and Bellono, N.W. (2025). A host organelle integrates stolen
507 chloroplasts for animal photosynthesis. Cell *188*, 5266-5277.e13.
508 https://doi.org/10.1016/j.cell.2025.06.003.

509 40. Seidel, T., Schnitzer, D., Golldack, D., Sauer, M., and Dietz, K.-J. (2008). Organelle-specific
510 isoenzymes of plant V-ATPase as revealed by in vivo-FRET analysis. BMC Cell Biol *9*, 28.
511 https://doi.org/10.1186/1471-2121-9-28.

512 41. Shimizu, K., Amo, Y.D., Brzezinski, M.A., Stucky, G.D., and Morse, D.E. (2001). A novel
513 fluorescent silica tracer for biological silicification studies. Chemistry & Biology *8*, 1051–1060.
514 https://doi.org/10.1016/S1074-5521(01)00072-2.

515 42. Dröse, S., and Altendorf, K. (1997). Bafilomycins and concanamycins as inhibitors of V-
516 ATPases and P-ATPases. J Exp Biol *200*, 1–8. https://doi.org/10.1242/jeb.200.1.1.

517 43. Huss, M., Ingenhorst, G., König, S., Gaßel, M., Dröse, S., Zeeck, A., Altendorf, K., and
518 Wieczorek, H. (2002). Concanamycin A, the Specific Inhibitor of V-ATPases, Binds to the Vo
519 Subunit c *. Journal of Biological Chemistry *277*, 40544–40548.
520 https://doi.org/10.1074/jbc.M207345200.

521 44. Vrieling, E.G., Gieskes, W.W.C., and Beelen, T.P.M. (1999). SILICON DEPOSITION IN
522 DIATOMS: CONTROL BY THE pH INSIDE THE SILICON DEPOSITION VESICLE. Journal of
523 Phycology *35*, 548–559. https://doi.org/10.1046/j.1529-8817.1999.3530548.x.

524 45. Mejía, L.M., Isensee, K., Méndez-Vicente, A., Pisonero, J., Shimizu, N., González, C.,
525 Monteleone, B., and Stoll, H. (2013). B content and Si/C ratios from cultured diatoms
526 (*Thalassiosira pseudonana* and *Thalassiosira weissflogii*): Relationship to seawater pH and
527 diatom carbon acquisition. Geochimica et Cosmochimica Acta *123*, 322–337.
528 https://doi.org/10.1016/j.gca.2013.06.011.

529 46. Baxter, I.R., Young, J.C., Armstrong, G., Foster, N., Bogenschutz, N., Cordova, T., Peer, W.A.,
530 Hazen, S.P., Murphy, A.S., and Harper, J.F. (2005). A plasma membrane H+-ATPase is
531 required for the formation of proanthocyanidins in the seed coat endothelium of Arabidopsis
532 thaliana. Proceedings of the National Academy of Sciences *102*, 2649–2654.
533 https://doi.org/10.1073/pnas.0406377102.

534 47. Mesdaghi, S., Murphy, D.L., Simpkin, A.J., and Rigden, D.J. (2023). Structural insights into
535 pink-eyed dilution protein (Oca2). Biosci Rep *43*, BSR20230060.
536 https://doi.org/10.1042/BSR20230060.

537 48. Kondo, T., Namiki, T., Coelho, S.G., Valencia, J.C., and Hearing, V.J. (2015). Oculocutaneous
538 albinism: Developing novel antibodies targeting the proteins associated with OCA2 and

539 OCA4. Journal of Dermatological Science *77*, 21–27.
540 https://doi.org/10.1016/j.jdermsci.2014.11.006.

541 49. Coskun, D., Deshmukh, R., Shivaraj, S.M., Isenring, P., and Bélanger, R.R. (2021). Lsi2: A
542 black box in plant silicon transport. Plant Soil *466*, 1–20. https://doi.org/10.1007/s11104-
543 021-05061-1.

544 50. Bellono, N.W., Escobar, I.E., Lefkovith, A.J., Marks, M.S., and Oancea, E. (2014). An
545 intracellular anion channel critical for pigmentation. eLife *3*, e04543.
546 https://doi.org/10.7554/eLife.04543.

547 51. Stauber, T., and Jentsch, T.J. (2013). Chloride in Vesicular Trafficking and Function. Annual
548 Review of Physiology *75*, 453–477. https://doi.org/10.1146/annurev-physiol-030212-183702.

549 52. Kahn, A.S., and Leys, S.P. (2017). Spicule and flagellated chamber formation in a growth
550 zone of Aphrocallistes vastus (Porifera, Hexactinellida). Invertebrate Biology *136*, 22–30.
551 https://doi.org/10.1111/ivb.12155.

552 53. Schröder, H.-C., Perović-Ottstadt, S., Rothenberger, M., Wiens, M., Schwertner, H., Batel, R.,
553 Korzhev, M., Müller, I.M., and Müller, W.E.G. (2004). Silica transport in the demosponge
554 Suberites domuncula: fluorescence emission analysis using the PDMPO probe and cloning of
555 a potential transporter. Biochem J *381*, 665–673. https://doi.org/10.1042/BJ20040463.

556 54. Forgac, M. (2007). Vacuolar ATPases: rotary proton pumps in physiology and
557 pathophysiology. Nat Rev Mol Cell Biol *8*, 917–929. https://doi.org/10.1038/nrm2272.

558 55. Ahearn, G.A., Sterling, K.M., Mandal, P.K., and Roggenbeck, B. (2010). Heavy Metal
559 Transport and Detoxification by Crustacean Epithelial Lysosomes. In Epithelial Transport
560 Physiology, G. A. Gerencser, ed. (Humana Press), pp. 49–71. https://doi.org/10.1007/978-1-
561 60327-229-2_3.

562 56. Wang, W.-X., Yang, Y., Guo, X., He, M., Guo, F., and Ke, C. (2011). Copper and zinc
563 contamination in oysters: subcellular distribution and detoxification. Environ Toxicol Chem
564 *30*, 1767–1774. https://doi.org/10.1002/etc.571.

565 57. Engel, D.W. (1983). The intracellular partitioning of trace metals in marine shellfish. Sci
566 Total Environ *28*, 129–140. https://doi.org/10.1016/s0048-9697(83)80013-8.

567 58. Subcellular compartmentalization of Cd and Zn in two bivalves. I. Significance of metal-
568 sensitive fractions (MSF) and biologically detoxified metal (BDM) | U.S. Geological Survey
569 https://www.usgs.gov/publications/subcellular-compartmentalization-cd-and-zn-two-
570 bivalves-i-significance-metal-sensitive.

571 59. Howard, B., Mitchell, P.C., Ritchie, A., Simkiss, K., and Taylor, M. (1981). The composition of
572 intracellular granules from the metal-accumulating cells of the common garden snail (Helix
573 aspersa). Biochem J *194*, 507–511. https://doi.org/10.1042/bj1940507.

574 60. Desouky, M.M.A. (2006). Tissue distribution and subcellular localization of trace metals in
575 the pond snail Lymnaea stagnalis with special reference to the role of lysosomal granules in
576 metal sequestration. Aquat Toxicol *77*, 143–152.
577 https://doi.org/10.1016/j.aquatox.2005.11.009.

578 61. Ballan-Dufrançais, C. (2002). Localization of metals in cells of pterygote insects. Microsc Res
579 Tech *56*, 403–420. https://doi.org/10.1002/jemt.10041.

580 62. Pigino, G., Migliorini, M., Paccagnini, E., and Bernini, F. (2006). Localisation of heavy metals
581 in the midgut epithelial cells of Xenillus tegeocranus (Hermann, 1804) (Acari: Oribatida).
582 Ecotoxicol Environ Saf *64*, 257–263. https://doi.org/10.1016/j.ecoenv.2005.12.012.

583 63. Blaby-Haas, C.E., and Merchant, S.S. (2014). Lysosome-related Organelles as Mediators of
584 Metal Homeostasis. J Biol Chem *289*, 28129–28136.
585 https://doi.org/10.1074/jbc.R114.592618.

586 64. Sterling, K.M., Mandal, P.K., Roggenbeck, B.A., Ahearn, S.E., Gerencser, G.A., and Ahearn,
587 G.A. (2007). Heavy metal detoxification in crustacean epithelial lysosomes: role of anions in
588 the compartmentalization process. J Exp Biol *210*, 3484–3493.
589 https://doi.org/10.1242/jeb.008300.

590 65. Simkiss, K. (1977). Biomineralization and detoxification. Calc. Tis Res. *24*, 199–200.
591 https://doi.org/10.1007/BF02223316.

592 66. Carney, C.K., Harry, S.R., Sewell, S.L., and Wright, D.W. (2007). Detoxification Biominerals. In
593 Biomineralization I: Crystallization and Self-Organization Process, K. Naka, ed. (Springer), pp.
594 155–185. https://doi.org/10.1007/128_050.

595 67. Li, X., Sun, M., Zhang, L., Finlay, R.D., Liu, R., and Lian, B. (2022). Widespread bacterial
596 responses and their mechanism of bacterial metallogenic detoxification under high
597 concentrations of heavy metals. Ecotoxicol Environ Saf *246*, 114193.
598 https://doi.org/10.1016/j.ecoenv.2022.114193.

599 68. Tsukuba, T., Sakai, E., Nishishita, K., Kadowaki, T., and Okamoto, K. (2017). New functions of
600 lysosomes in bone cells. Journal of Oral Biosciences *59*, 92–95.
601 https://doi.org/10.1016/j.job.2017.01.004.

602 69. James, A., Hendrixson, J.A., Kadhim, I., Marques-Carvalho, A., Laster, J., Crawford, J.,
603 Thostenson, J., Wanchai, V., Sato, A.Y., Nookaew, I., et al. (2025). Elevation of master
604 autophagy regulator *Tfeb* in osteoblast lineage cells increases bone mass and strength. JCI
605 Insight *10*. https://doi.org/10.1172/jci.insight.191688.

606 70. Murdock, D.J.E. (2020). The 'biomineralization toolkit' and the origin of animal skeletons.
607 Biological Reviews *95*, 1372–1392. https://doi.org/10.1111/brv.12614.

71. Sciani, J.M., Antoniazzi, M.M., Neves, A. da C., and Pimenta, D.C. (2013). Cathepsin B/X is secreted by Echinometra lucunter sea urchin spines, a structure rich in granular cells and toxins. J Venom Anim Toxins Incl Trop Dis *19*, 33. https://doi.org/10.1186/1678-9199-19-33.

72. Levy, S., Elek, A., Grau-Bové, X., Menéndez-Bravo, S., Iglesias, M., Tanay, A., Mass, T., and Sebé-Pedrós, A. (2021). A stony coral cell atlas illuminates the molecular and cellular basis of coral symbiosis, calcification, and immunity. Cell *184*, 2973-2987.e18. https://doi.org/10.1016/j.cell.2021.04.005.

73. Müller, W.E.G., Wang, X., Kropf, K., Ushijima, H., Geurtsen, W., Eckert, C., Tahir, M.N., Tremel, W., Boreiko, A., Schloßmacher, U., et al. (2008). Bioorganic/inorganic hybrid composition of sponge spicules: Matrix of the giant spicules and of the comitalia of the deep sea hexactinellid *Monorhaphis*. Journal of Structural Biology *161*, 188–203. https://doi.org/10.1016/j.jsb.2007.10.009.

74. Povarova, N.V., Barinov, N.A., Baranov, M.S., Markina, N.M., Varizhuk, A.M., Pozmogova, G.E., Klinov, D.V., Kozhemyako, V.B., and Lukyanov, K.A. (2018). Efficient silica synthesis from tetra(glycerol)orthosilicate with cathepsin- and silicatein-like proteins. Sci Rep *8*, 16759. https://doi.org/10.1038/s41598-018-34965-9.

75. Görlich, S., Samuel, A.J., Best, R.J., Seidel, R., Vacelet, J., Leonarski, F.K., Tomizaki, T., Rellinghaus, B., Pohl, D., and Zlotnikov, I. (2020). Natural hybrid silica/protein superstructure at atomic resolution. Proceedings of the National Academy of Sciences *117*, 31088–31093. https://doi.org/10.1073/pnas.2019140117.

76. Pozzolini, M., Mikšík, I., Ghignone, S., Oliveri, C., Tassara, E., and Giovine, M. (2022). The Lysosome Origin of Biosilica Machinery in the Demospongiae Model Petrosia ficiformis (Poiret, 1789). Front. Mar. Sci. *9*. https://doi.org/10.3389/fmars.2022.850653.

77. More, K.J., Kaufman, J.G.G., Dacks, J.B., and Manna, P.T. (2024). Evolutionary origins of the lysosome-related organelle sorting machinery reveal ancient homology in post-endosome trafficking pathways. Proc Natl Acad Sci U S A *121*, e2403601121. https://doi.org/10.1073/pnas.2403601121.

78. Armstrong, R.A., Lee, C., Hedges, J.I., Honjo, S., and Wakeham, S.G. (2001). A new, mechanistic model for organic carbon fluxes in the ocean based on the quantitative association of POC with ballast minerals. Deep Sea Research Part II: Topical Studies in Oceanography *49*, 219–236. https://doi.org/10.1016/S0967-0645(01)00101-1.

79. Aldridge, D., Beer, C.J., and Purdie, D.A. (2012). Calcification in the planktonic foraminifera *Globigerina bulloides* linked to phosphate concentrations in surface waters of the North Atlantic Ocean. Biogeosciences *9*, 1725–1739. https://doi.org/10.5194/bg-9-1725-2012.

80. Steenwyk, J.L., and King, N. (2025). Integrative phylogenomics positions sponges at the root of the animal tree. Science *390*, 751–756. https://doi.org/10.1126/science.adw9456.

644 81. Nichols, S. (2023). Growing freshwater sponges from gemmules in the laboratory.

645 82. Armstrong, E.J., Roa, J.N., Stillman, J.H., and Tresguerres, M. (2018). Symbiont
646 photosynthesis in giant clams is promoted by V-type H+-ATPase from host cells. J Exp Biol
647 *221*, jeb177220. https://doi.org/10.1242/jeb.177220.

648 83. Damsgaard, C., Lauridsen, H., Harter, T.S., Kwan, G.T., Thomsen, J.S., Funder, A.M., Supuran,
649 C.T., Tresguerres, M., Matthews, P.G., and Brauner, C.J. (2020). A novel acidification
650 mechanism for greatly enhanced oxygen supply to the fish retina. eLife *9*, e58995.
651 https://doi.org/10.7554/eLife.58995.

652 84. Roa, J.N., and Tresguerres, M. (2016). Soluble adenylyl cyclase is an acid-base sensor in
653 epithelial base-secreting cells. American Journal of Physiology-Cell Physiology *311*, C340–
654 C349. https://doi.org/10.1152/ajpcell.00089.2016.

655 85. Nichols, S. (2023). Fixation and staining of gemmule-hatched Ephydatia muelleri for
656 fluorescence microscopy v1. Preprint, https://doi.org/10.17504/protocols.io.j8nlkwnx6l5r/v1
657 https://doi.org/10.17504/protocols.io.j8nlkwnx6l5r/v1.

658 86. Kuehn, E., Clausen, D.S., Null, R.W., Metzger, B.M., Willis, A.D., and Özpolat, B.D. (2022).
659 Segment number threshold determines juvenile onset of germline cluster expansion in
660 Platynereis dumerilii. J Exp Zool B Mol Dev Evol *338*, 225–240.
661 https://doi.org/10.1002/jez.b.23100.

662 87. Choi, H.M.T., Schwarzkopf, M., Fornace, M.E., Acharya, A., Artavanis, G., Stegmaier, J.,
663 Cunha, A., and Pierce, N.A. (2018). Third-generation in situ hybridization chain reaction:
664 multiplexed, quantitative, sensitive, versatile, robust. Development *145*, dev165753.
665 https://doi.org/10.1242/dev.165753.

666 88. Wang, Y., Liu, X., Zeng, Y., Saka, S.K., Xie, W., Goldaracena, I., Kohman, R.E., Yin, P., and
667 Church, G.M. (2024). Multiplexed in situ protein imaging using DNA-barcoded antibodies
668 with extended hybridization chain reactions. Nucleic Acids Res *52*, e71.
669 https://doi.org/10.1093/nar/gkae592.

670 89. Tsuneoka, Y., and Funato, H. (2020). Modified in situ Hybridization Chain Reaction Using
671 Short Hairpin DNAs. Front Mol Neurosci *13*, 75. https://doi.org/10.3389/fnmol.2020.00075.

672 90. Nichols, S. (2023). HCR-fluorescent in situ hybridization (HCR-FISH) of gemmule-hatched
673 freshwater sponges.

674
675

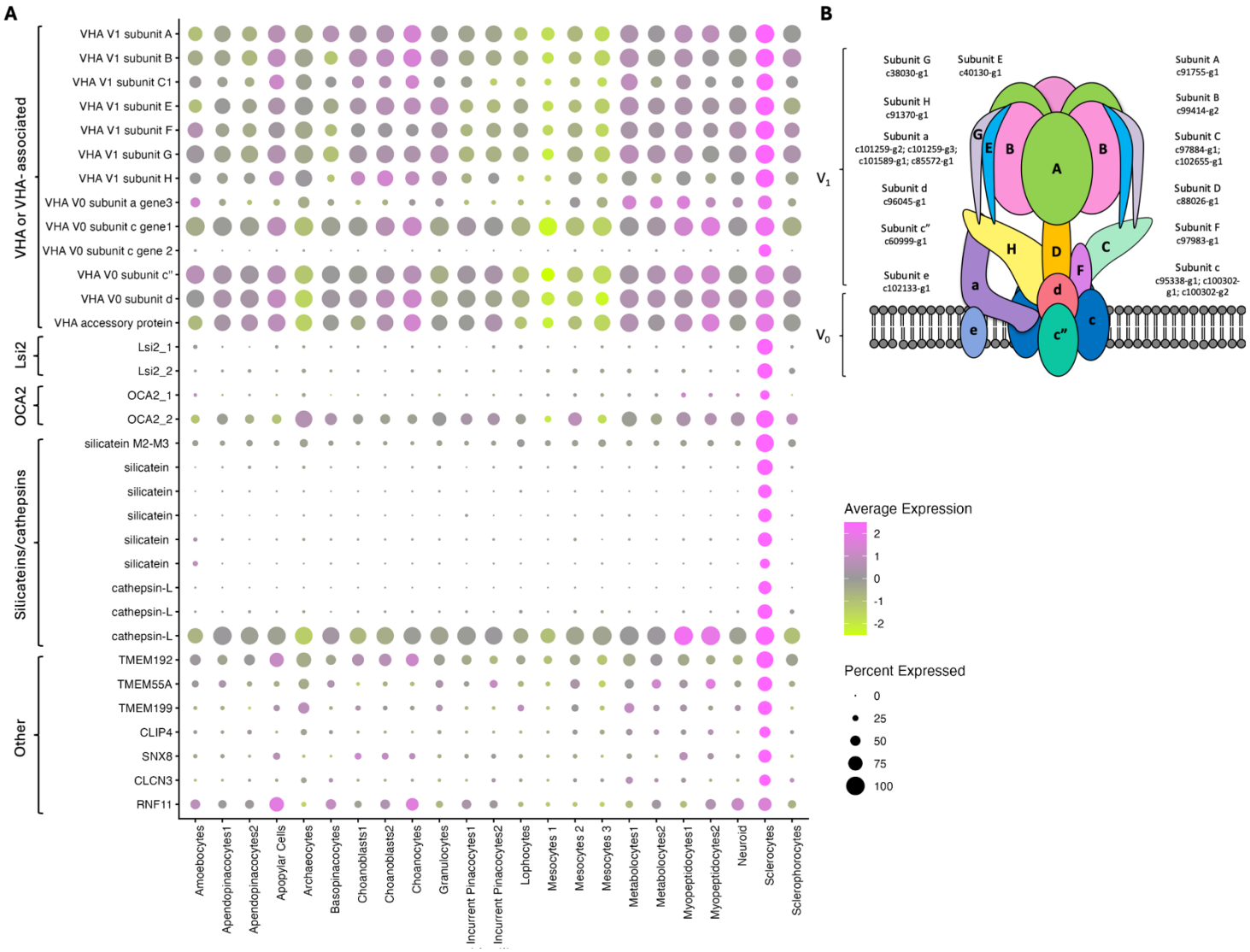

Figure 1. Single-cell RNA-Seq expression of lysosome-related sclerocyte markers. (A) Heatmap showing expression of genes upregulated (log2fold>1) in sclerocytes that are linked with lysosomal function across *S. lacustris* cell types (single-cell RNASeq data from Musser et al., 2021). Note: not all VHA subunits are present here as they did not all make the cutoff log2fold cutoff. (B) Cartoon of VHA showing *S. lacustris* genes encoding each subunit.

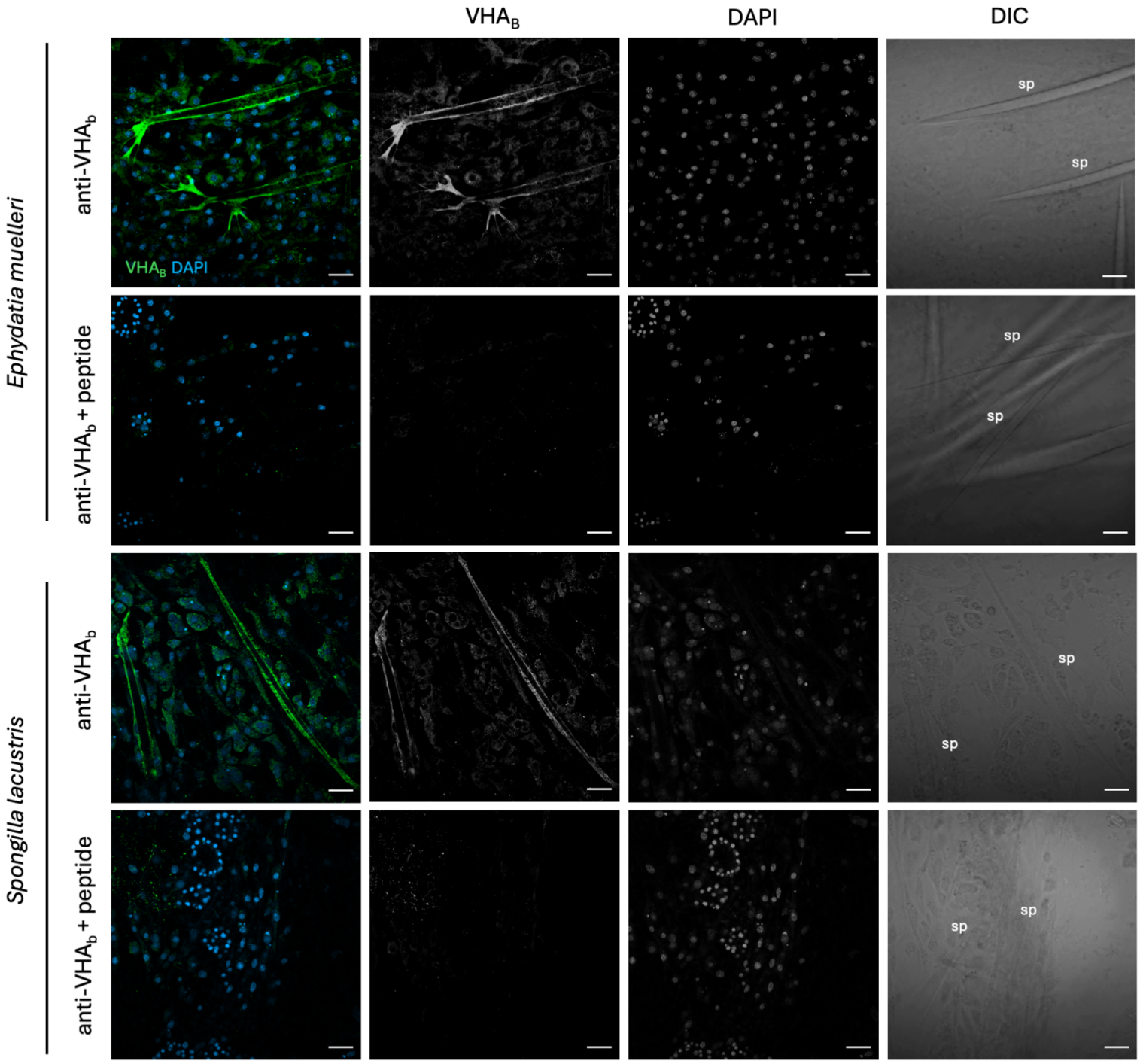

Figure 2. VHA localization in *Ephydatia muelleri* and *Spongilla lacustris*. Immunohistochemical localization of VHA_B in *E. muelleri* and *S. lacustris* sponges incubated with anti-VHA_B antibody or anti-VHA_B antibody with excess peptide (peptide pre-absorption control). VHA_B in green, DAPI in blue. VHA_B, DAPI, and DIC channels are also shown separately. All images except DIC are orthogonal projections. Scale bars: 20 µm. sp; spicules.

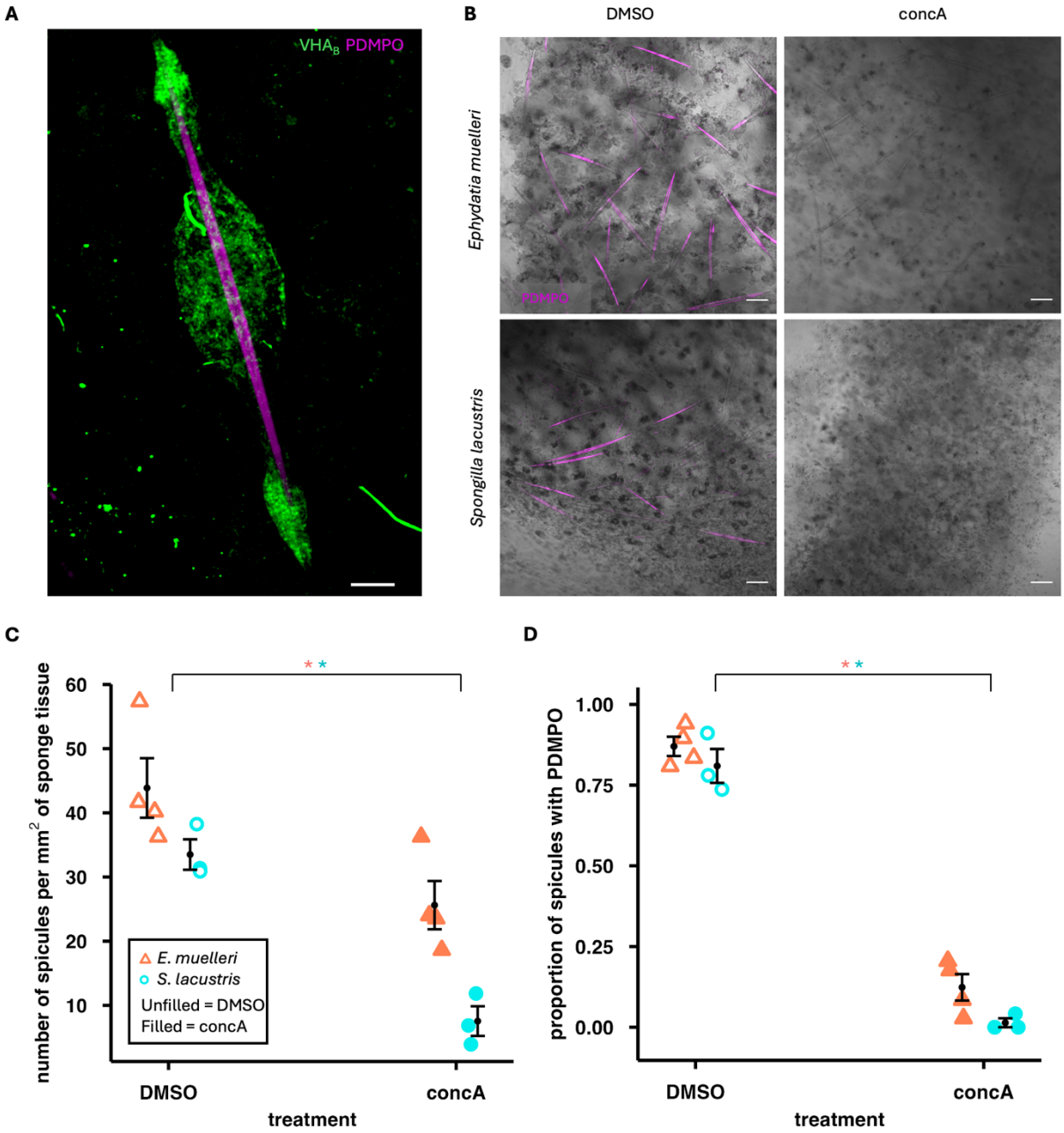

Figure 3. Essential role of VHA in spiculogenesis in *Ephydatia muelleri* and *Spongilla lacustris.* (A) Airyscan confocal image showing VHA$_B$ localization around *E. muelleri* spicule labelled with PDMPO (B) Representative images of PDMPO fluorescence of spicules in sponges incubated with DMSO or 100 nM concA for 24 hours. (C) Dot plot depicting the number of spicules per mm^2 of sponge tissue incubated with DMSO or 100 nM concA for 24 hours with error bars. (D) Dot plot depicting average proportion of spicules that showed PDMPO fluorescence in sponges incubated with DMSO or 100 nM concA for 24 hours with error bars. *E. muelleri* in red (n=4) and *S. lacustris* in cyan (n=3). Asterisks denote statistical significance (t test, p-value < 0.05). VHA$_B$ in green, PDMPO in magenta. Scale bars in (A): 5 µm and (B): 50 µm.

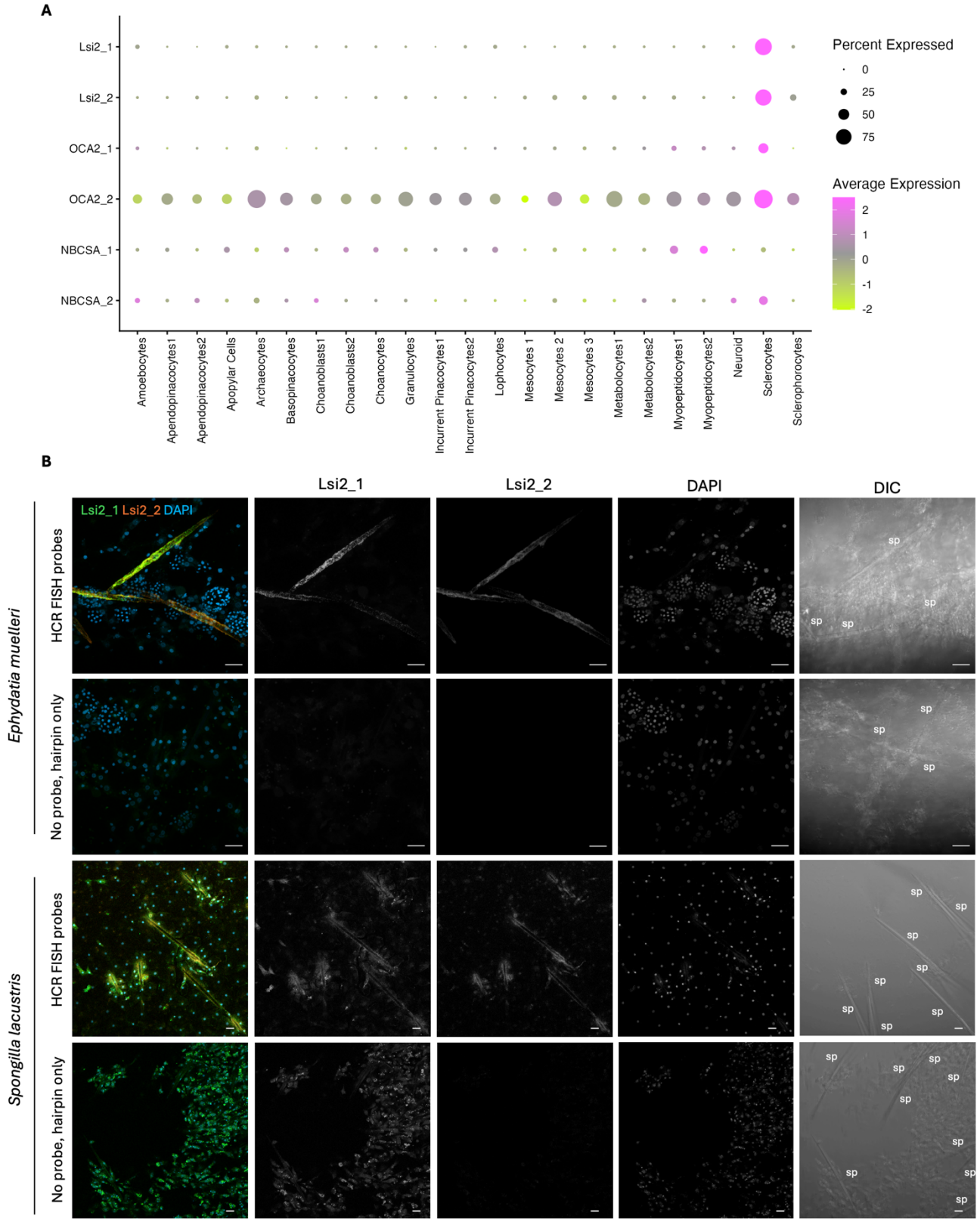

Figure 4. Gene expression of Lsi2 genes in *Ephydatia muelleri* and *Spongilla lacustris*. (A) Heatmap showing expression of Lsi2, OCA2, and [$Na^+/HCO_3^-[Si(OH)_4]$] co-transporter (NBCSA) genes in *S. lacustris* cell types. (B) HCR-FISH in *E. muelleri* and *S. lacustris* sponges incubated with probes designed against Lsi2_1 and Lsi2_2 genes. Lsi2_1 in green, Lsi2_2 in orange, DAPI in blue. Lsi2_1, Lsi2_2, DAPI, and DIC channels are also shown separately in grayscale. All images are orthogonal projections. Scale bars: 20 µm. sp; spicules

Supplementary figures

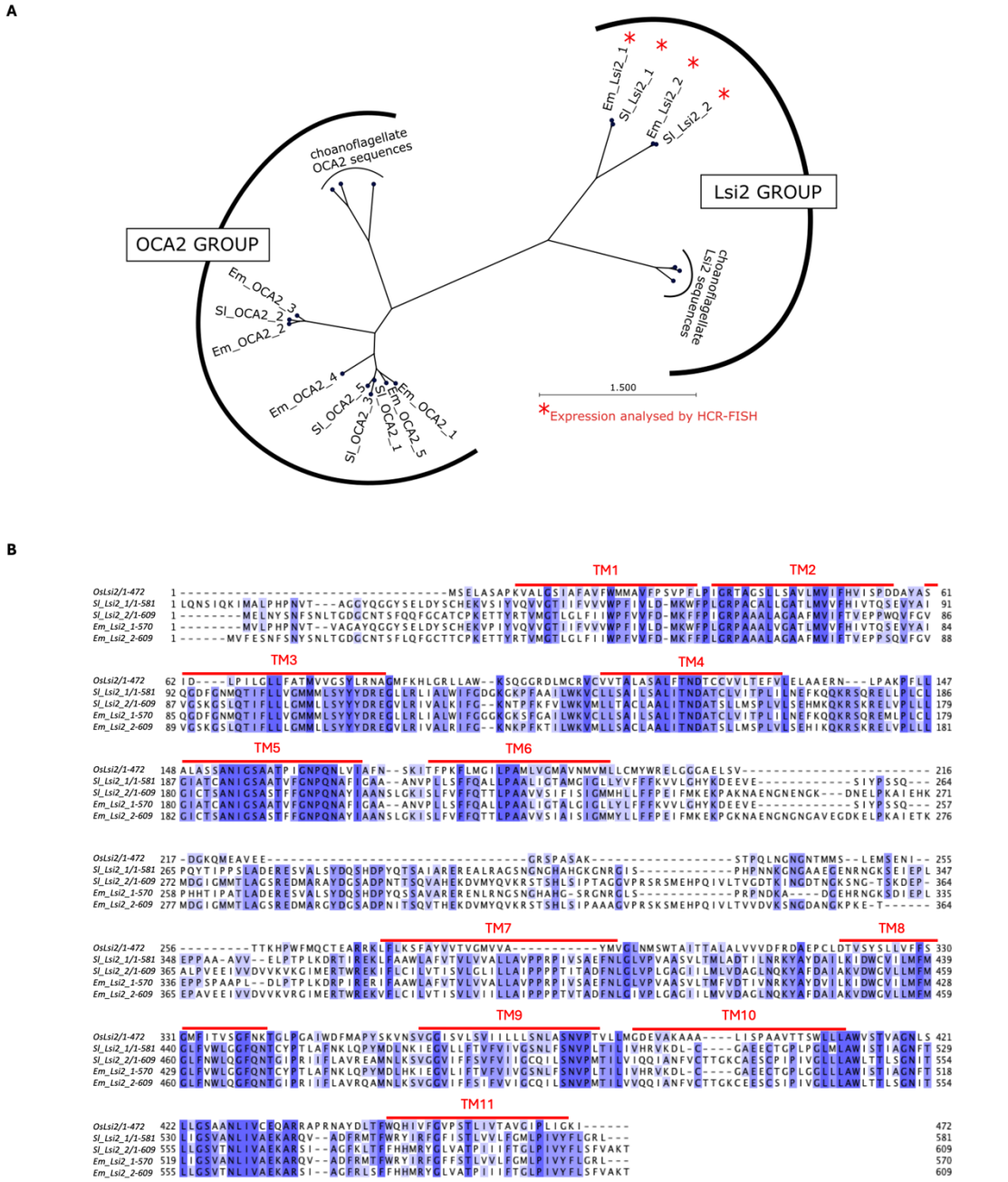

Supplementary Figure 1. Phylogenetic and structural analysis of Lsi2/OCA2 homologs. (A) Lsi2 and OCA2 homologs were identified in *Ephydatia muelleri* (abbreviated Em) and *Spongilla lacustris* (abbreviated Sl) genomic and transcriptomic datasets by BLAST searches using choanoflagellate sequences from Marron *et al.* and by extraction of candidate orthogroups from OrthoFinder. Protein sequences were aligned with MAFFT using the DASH structure-guided alignment mode, after which DASH profile sequences were removed. The alignment was trimmed with ClipKIT to retain phylogenetically informative sites, and a maximum-likelihood phylogeny was inferred using IQ-TREE with automated model selection and branch support assessed by 1,000 ultrafast bootstraps and 1,000 SH-aLRT replicates. (B) Sequence alignment of *OsLsi2* gene from rice (*Oryza sativa),* Lsi2_1 and 2 from *E muelleri*, and Lsi2_1 and 2 from *S. lacustris.* Alignment shaded from light blue to dark blue based on percentage identity similarity. 11 predicted transmembrane (TM) domains in red (based on Ma et al., 2007). Sequence alignments were done on Clustal Omega and visualized using Jalview.

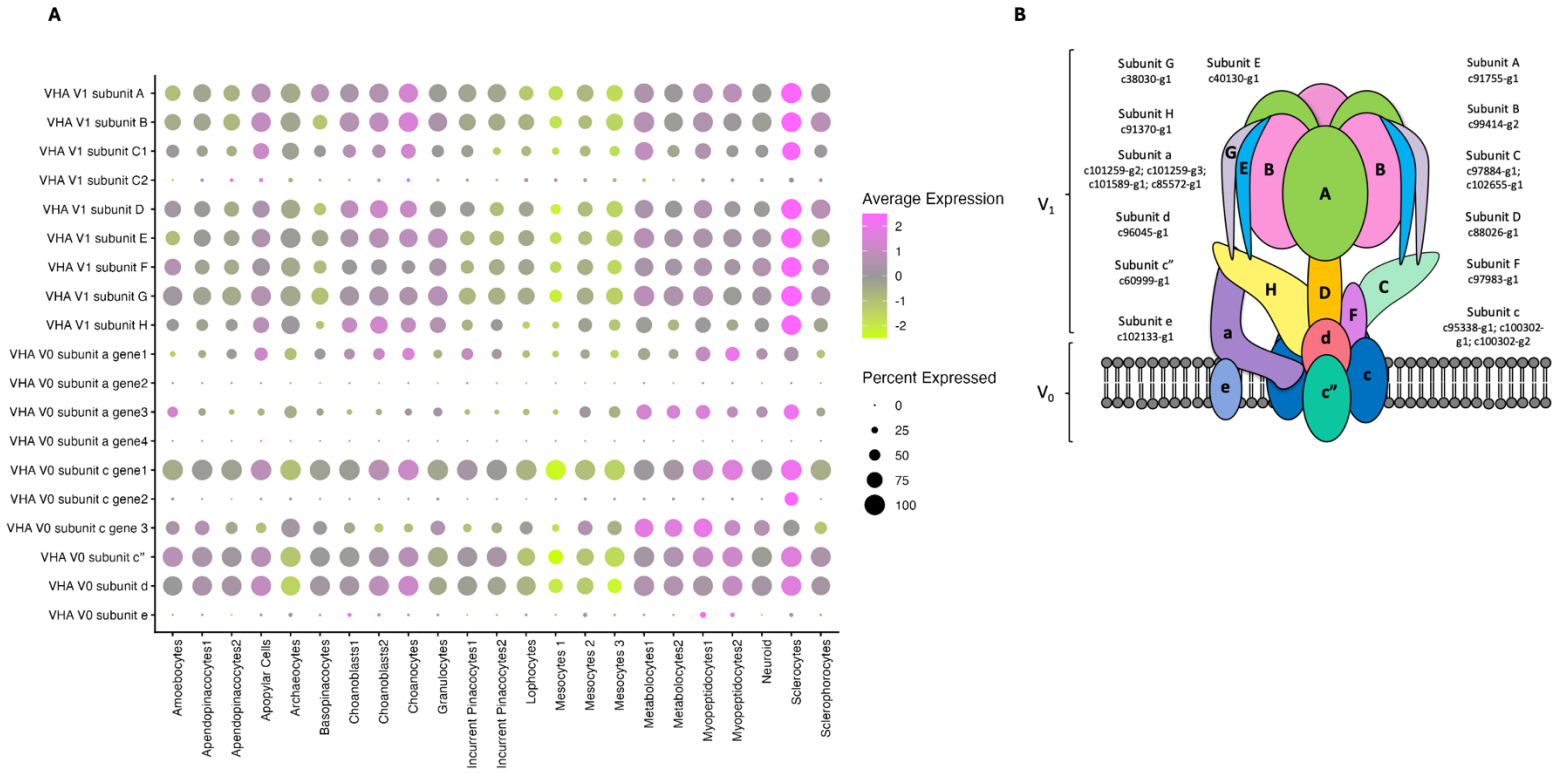

Supplementary Figure 2. Single-cell RNA-Seq expression of VHA subunits in *S. lacustris.* (A) Heatmap showing expression of genes encoding VHA subunits in *S. lacustris* cell types (single-cell RNASeq data from Musser et al., 2021). Highest expression of almost all VHA subunits occurs in sclerocytes. (B) Cartoon of VHA showing *S. lacustris* genes encoding each subunit.

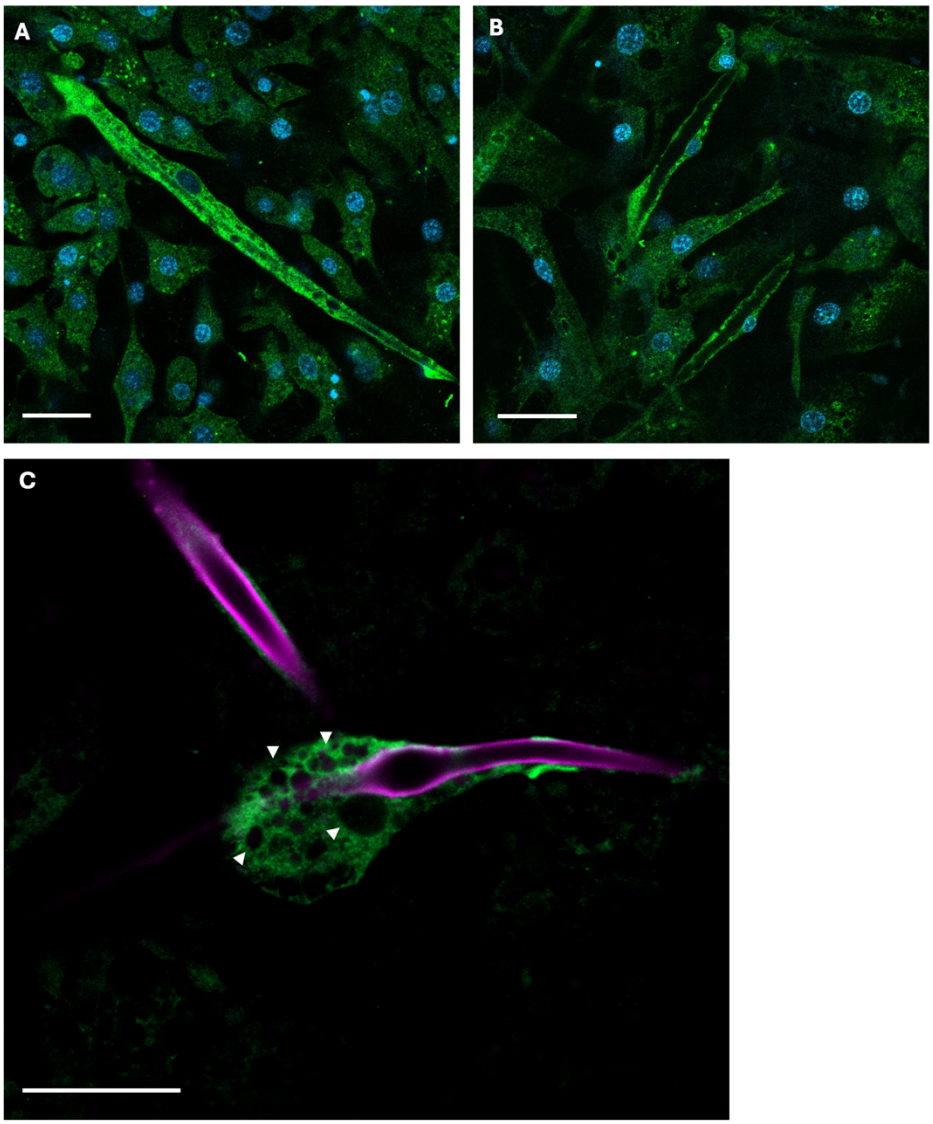

Supplementary Figure 3. VHA localization at sclerocyte SDV and within cytoplasm in *S. lacustris*. (A, B) Confocal microscopy showing VHA_B immunolabeling in *E. muelleri* sclerocytes surrounding spicules and within cytoplasm. (C) Airyscan confocal image showing VHA_B localization around *E. muelleri* spicule labelled with PDMPO. Arrows indicate vesicles surrounded by VHA_B. VHA_B in green, DAPI in blue, PDMPO in magenta. Scale bars: 20 µm

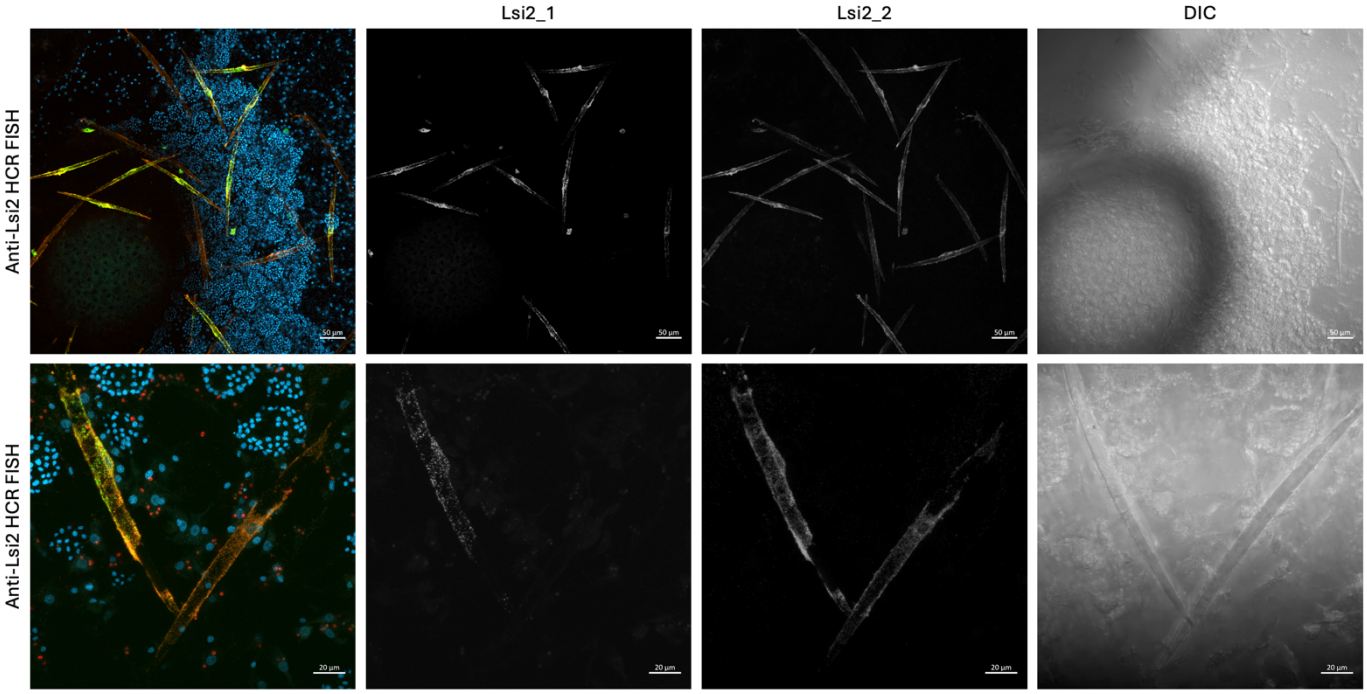

Supplementary Figure 4. HCR-FISH in *E. muelleri* sponges incubated with probes against Lsi2_1 and Lsi2_2 genes. Representative images showing more ubiquitous Lsi2_2 expression around spicules than Lsi2_1. Lsi2_1 in green, Lsi2_2 in orange, DAPI in blue. Lsi2_1, Lsi2_2, DAPI, and DIC channels are also shown separately in grayscale. Lsi1_1 and Lsi2_2 probes imaged at same laser intensity and gain. All images are orthogonal projections.

A

```
Homo sapiens    135  KGPVVMAEDFLDINGQPINPHSRIYPEEMIQTGISPIDVMNSIARGQKIPIFSAAGLPHNEIAAQICRQAGLVKKS-KAVLDYHDDNFAIVFAAMGVNMETARFFKSDFEQNGTMGNVCL  253
S. pistillata   124  KGPAVMAEDFLDIQGQPINPWSRIYPEEMIQTGISAIDTMNSIARGQKIPIFSAAGLPHNDIAAQICRQAGLVKFK-KGVMDDHSDNFAIVFAAMGVNMETARFFKQDFEENGSMENVCL  242
S. lacustris    133  KGPNILAEDFLDIQGQPINPWSRIYPEEMIQTGISAIDTMNSIARGQKIPIFSAAGLPHNDIAAQICRQGGLVKQTPKGVIDDHEANFAIVFAAMGVNMETARFFKQDFEENGSMENVCL  252
E. muelleri     133  KGPNILAEDFLDIQGQPINPWSRIYPEEMIQTGISAIDTMNSIARGQKIPIFSAAGLPHNDIAAQICRQGGLVKQTPKGVIDDHEANFAIVFAAMGVNMETARFFKQDFEENGSMENVCL  252

Homo sapiens    254  FLNLANDPTIERIITPRLALTTAEFLAYQCEKHVLVILTDMSSYAEALREVSAAREEVPGRRGFPGYMYTDLATIYERAGRVEGRGGSITQIPILTMPNDDITHPIPDLTGFITEGQIYV  373
S. pistillata   243  FLNLANDPTIERIITPRLALTTAEFLAYQCENHVLVILTDMSSYAEALREVSAAREEVPGRRGFPGYMYTDLATIYERAGRVEGRNGSITQIPILTMPNDDITHPIPDLTGYITEGQIYV  362
S. lacustris    253  FLNLANDPTIERIITPRLALTTAEFLAYQCEKHVLVILTDMSSYAEALREVSAAREEVPGRRGFPGYMYTDLATIYERAGRVEGRNGSITQIPILTMPNDDITHPIPDLTGYITEGQIYV  372
E. muelleri     253  FLNLANDPTIERIITPRLALTTAEFLAYQCEKHVLVILTDMSSYAEALREVSAAREEVPGRRGFPGYMYTDLATIYERAGRVEGRNGSITQIPILTMPNDDITHPIPDLTGYITEGQIYV  372

Homo sapiens    374  DRQLHNRQIYPPINVLPSLSRLMKSAIGEGMTRKDHGDVSNQLYACYAIGKDVQAMKAVVGEEALTSEDLLYLEFLQKFEKNFINQGPYENRSVFESLDLGWKLLRIFPKEMLKRIPQAV  493
S. pistillata   363  DRQLHNRQVYPPINVLPSLSRLMKSAIGEGMTRKDHADVSNQLYANYAIGKDVQAMKAVVGEEALTSEDLLYLEFLSKFEKNFITQGTYENRSVFDSLDIGWSLLRIFPKEMLKRIPQSI  482
S. lacustris    373  DRQLHNRQIYPPINVLPSLSRLMKSAIGDGMTRKDHADVSNQLYANYAIGKDVQAMKAVVGEEALTSEDKLYLEFLIKFEKNFITQGVYENRTVFESLEIGWQLLRIFPKEMLKRIPQSV  492
E. muelleri     373  DRQLHNRQIYPPINVLPSLSRLMKSAIGDGMTRRDHADVSNQLYANYAIGKDVQAMKAVVGEEALSSEDKLYLEFLQKFEKNFIAQGVYENRTVFESLEIGWQLLRIFPKEMLKRIPQAV  492

Homo sapiens    494  IDEFYSREG  502
S. pistillata   483  LAEYYPRDG  491
S. lacustris    493  LDEYYARD   500
E. muelleri     493  LDEYYARD   500
```

B

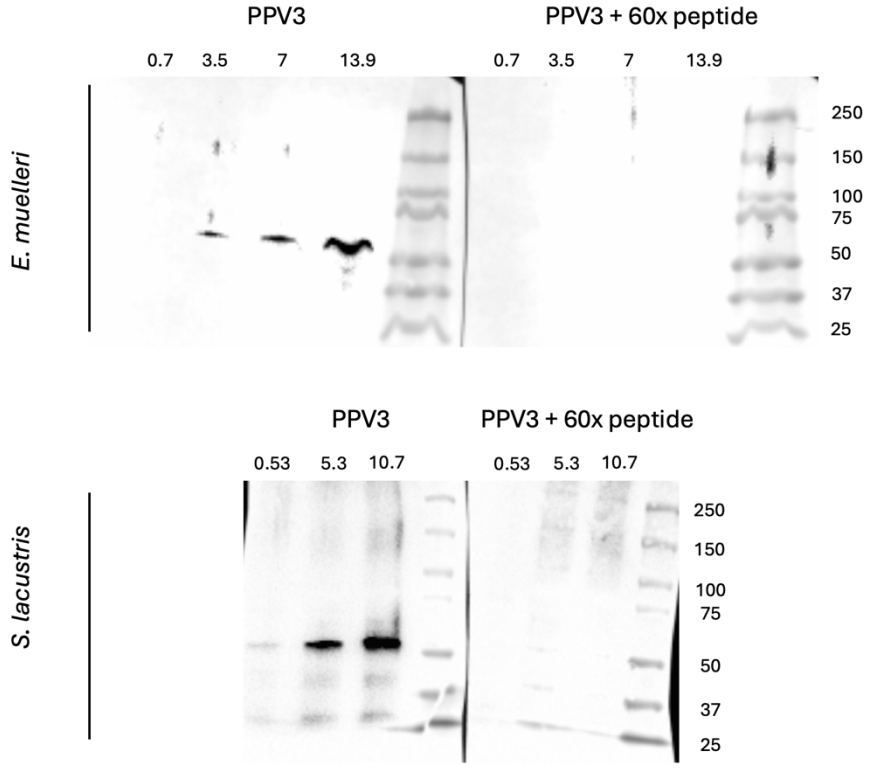

Supplementary Figure 5. VHA expression and conservation in sponges. (A) Alignment of the human VHA_B protein sequence with the coral *Stylophora pistillata, S. lacustris, and E. muelleri* VHA_B protein sequences. (B) Western blot detection of VHA in E. muelleri and S. lacustris using anti-VHA_B antibody, and anti-VHA_B antibody preabsorbed with 60x excess peptide on blots loaded with 0.7 µg, 3.5 µg, 7 µg, and 13.9 µg protein (*E. muelleri*) and 0.53 µg, 5.3 µg, and 10.7 µg protein (*S. lacustris*).

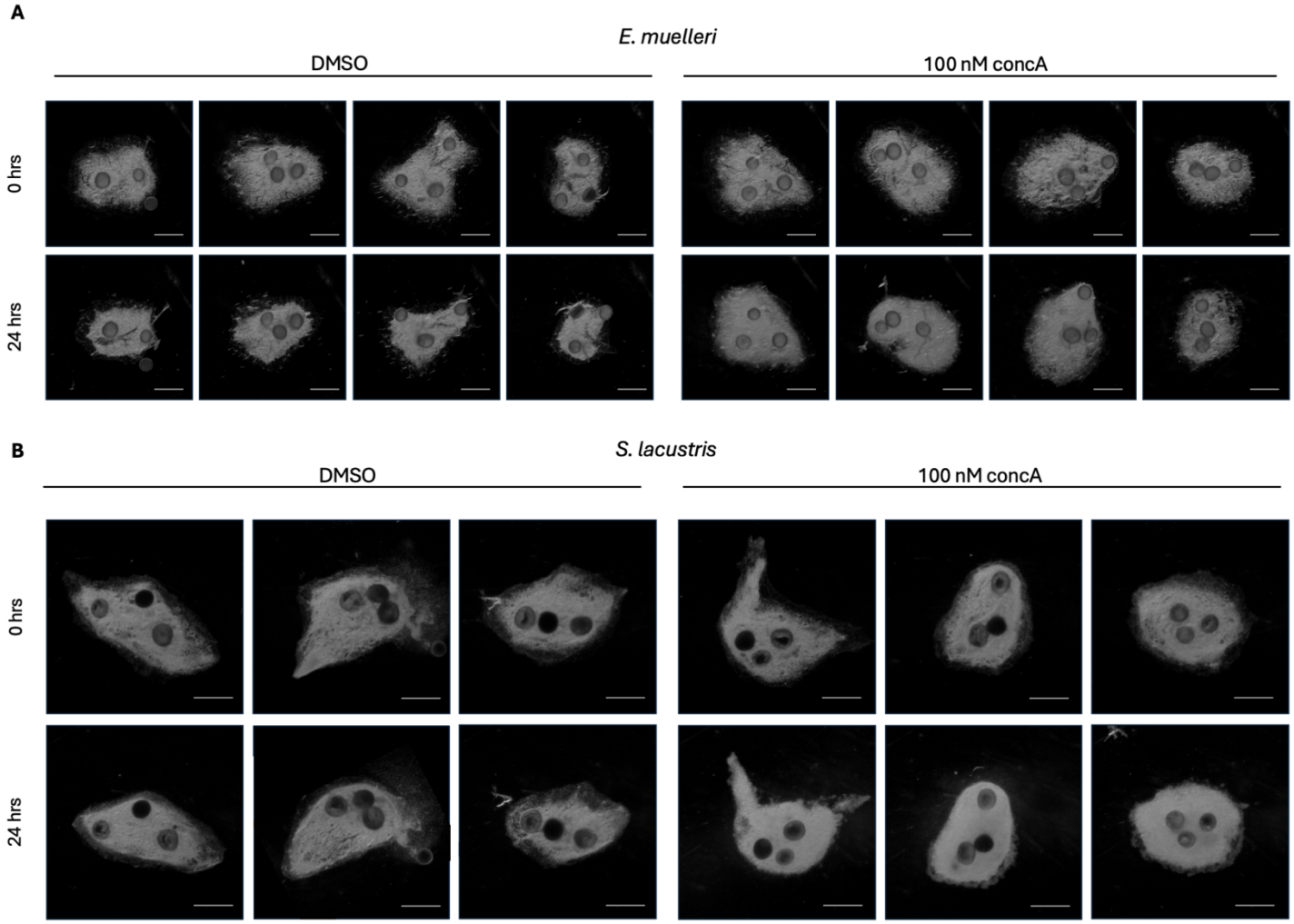

Supplementary Figure 6. Stereoscope images of *E. muelleri* and *S. lacustris* before and after concA treatment to assess viability. 4-day old sponges before and after 24 hr treatment with 1 uM PDMPO and DMSO or 100 nM concA followed by washout and replacement with spring water + 1uM PDMPO in (A) *E. muelleri* and (B*) S. lacustris.* Scale bars: 1 mm